Earth and Planetary Science Letters 503 (2018) 17–28

Contents lists available at ScienceDirect

Earth and Planetary Science Letters

www.elsevier.com/locate/epsl

Slip-partitioning above a shallow, weak décollement beneath the Indo-Burman accretionary prism

Paul M. Betka [a,*], Leonardo Seeber [a], Stuart N. Thomson [b], Michael S. Steckler [a], Ryan Sincavage [c], C. Zoramthara [d]

[a] Lamont-Doherty Earth Observatory, Columbia University, Palisades, NY, USA
[b] University of Arizona, Department of Geosciences, Tucson, AZ, USA
[c] Radford University, Geology Department, Radford, VA, USA
[d] Government Zirtiri Residential Science College, Geology Department, Aizawl, Mizoram, India

ARTICLE INFO

Article history:
Received 28 June 2018
Received in revised form 23 August 2018
Accepted 4 September 2018
Available online 27 September 2018
Editor: A. Yin

Keywords:
Indo-Burman ranges
subduction
fold belt
accretionary prism
Himalayas
slip partitioning

ABSTRACT

The Indo-Burman Ranges (IBR) are an ~375 km wide accretionary prism that accommodates oblique convergence of the ~13–20 km thick Ganges–Brahmaputra Delta on the Indian plate with the Shan Plateau to the east and Shillong massif to the north. The IBR are entirely subaerial and adjacent to one of the most densely populated (>140 M people) regions on the planet, with the potential to generate a $M_w \geq 8.2$ megathrust earthquake. To determine the kinematic evolution, décollement geometry, and geologic deformation rates near the front of the IBR, we combined geologic field mapping, detrital thermochronology, and structural analysis of eight antiforms that define the ~120 km wide outer belt. The antiforms are bivergent fault-propagation or detachment folds that record plane-strain and east-trending horizontal shortening perpendicular to the axial trace of the folds, indicating nearly full slip-partitioning with the fold-belt normal and parallel components of convergence dominating, respectively, the front and back of the IBR. At 24°N the antiforms have accommodated ~38.4 ± 16 km of shortening since ~8 Ma above a ~3–4 km deep, weak, subhorizontal décollement. Results indicate a shortening rate of ≥4.8 mm/yr, at least 28–37% of the arc-normal geodetic rate, and thrust front propagation rate of ≥15 km/Myr. The shallow décollement is laterally continuous with a regional detachment previously imaged by industry seismic reflection profiles to the west, north, and south of the study area. We interpret this décollement to be the up-dip part of the megathrust that has the potential to accommodate large coseismic slip during a great earthquake.

1. Introduction

The Indo-Burman Ranges (IBR, Fig. 1) are a west-directed fold-thrust belt located at the northern end of the Sunda subduction zone where it joins the Himalayan collisional orogen. Plate convergence between India and southeast Asia at the IBR trends north–northeast, highly oblique (~70°; 46 mm/yr) to the northerly trend of the plate margin (Nielsen et al., 2004; Rangin et al., 2013; Steckler et al., 2016). Where the subduction zone encounters the ~13–20 km thick Ganges–Brahmaputra Delta (GBD), the IBR widens to >300 km to accommodate the thickly sedimented margin. Oblique convergent margins commonly result in partitioning of the orogen-parallel and orogen-normal components of the plate motion (McCaffrey et al., 2000). Even in highly oblique settings, such as Sumatra, megathrust earthquakes occur and record slip that is oblique to the overall plate convergence vector, reflecting full to partial slip partitioning of the upper plate (Bradley et al., 2017 and references therein).

The degree of slip-partitioning and nature of the highly oblique India–Asia convergence at the IBR is controversial. One view proposes active subduction is highly partitioned between the frontal fold-thrust belt and dextral strike-slip faults in the internal part of the IBR (Satyabala, 1998; Nielson et al., 2004; Steckler et al., 2016). Another posits that the IBR is undergoing purely dextral strike-slip deformation with no active subduction (Rao and Kumar, 1999). Part of this controversy reflects the fact that structural geometry and kinematics of deformation across the frontal part of the IBR continue to be debated. For example, Maurin and Rangin (2009) consider the outer belt as a thin-skinned fold-belt that is overprinted by thick-skinned dextral transpressional deformation associated with an inferred, basement-involved fault that they call the Chittagong Coastal fault. Similarly, Rangin et al. (2013) in-

* Corresponding author.
E-mail address: pbetka@ldeo.columbia.edu (P.M. Betka).

https://doi.org/10.1016/j.epsl.2018.09.003
0012-821X/

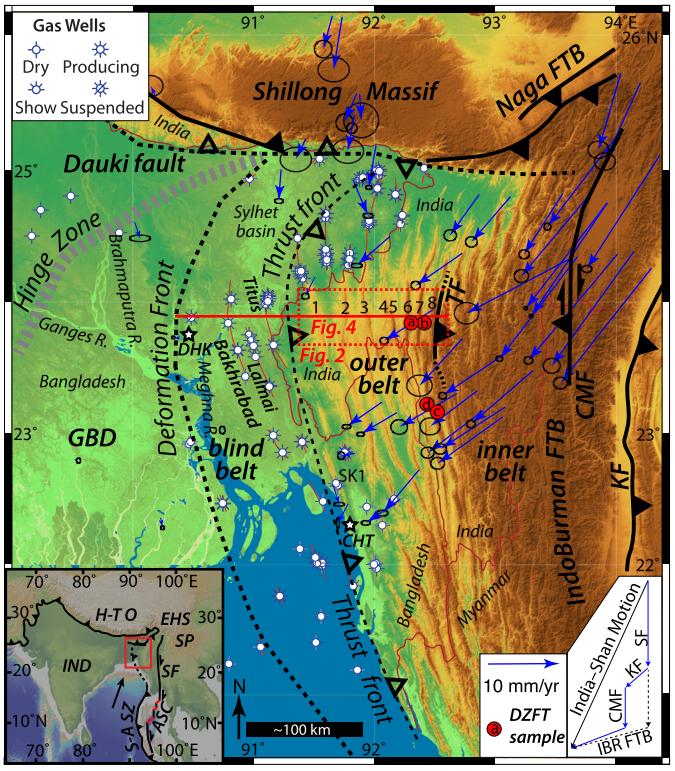

Fig. 1. Shaded relief map of the IBR showing GPS velocities in an Indian frame of reference and major structures (black lines, dashed where blind). The inset in lower right shows velocity triangles (inset vectors not to scale, dashed arrows show an alternative single fault model; Steckler et al., 2016). The deformation front (dashed black curve) marks the western limit of gentle, buried anticlines, based on exploration wells and industry seismic data (e.g., Imam and Hussain, 2002). The study area and location of Fig. 2 is shown with a red-dashed box. The solid red line shows the cross section location for Fig. 4. Black numerals 1–8 in the study area mark the location of antiforms A1–8. Red-colored circles with letters a–d show locations of dZFT samples (a) N386, (b) N357A, (c) MIZ05 and (d) MIZ06. Dark brown line shows international borders. Inset, lower left: tectonic setting of the IBR. The large black arrow gives the plate motion of India with respect to the Shan Plateau. Black and white stars labeled DHK and CHT mark the cities of Dhaka and Chittagong, respectively. Abbreviations: SK-1 – Sitakund 1 well; CMF – Churachandpur–Mao Fault; KF – Kabaw Fault; TF – Tut Fault; Inset: S–A SZ – Sumatra–Andaman subduction zone; ASC – Andaman spreading center; SF – Sagaing Fault; SP – Shan Plateau; EHS – Eastern Himalayan syntaxis; H–T O – Himalayan–Tibetan orogen; IND – Indian craton. (For interpretation of the colors in the figure(s), the reader is referred to the web version of this article.)

terpret the inner belt as a right lateral shear zone on the basis of strike-slip centroid moment tensor solutions from intermediate depth (30–100 km) earthquakes in the lower plate (cf. Rao and Kumar, 1999). Rangin et al. (2013) and Rangin (2017) also highlight submarine landslides at the shelf break offshore of western Myanmar to argue that shortening across the outer and blind belts is driven by gravity collapse.

Recent geodetic data from the IBR confirms that there is active convergence and that the plate motion is strongly partitioned at the latitude of the GBD. Between the active deformation front in Bangladesh (90.5°E) and the Shan Plateau in Myanmar (SP, 97.5°E) dextral shear is mostly absorbed by north-striking right-lateral faults in the internal part of the forearc, including the Sagaing and Churachandpur–Mao faults (SF and CMF, Fig. 1; Steckler et al., 2016; Sloan et al., 2017). Most of the 70° of the total obliquity is taken up between the SF and CMF, leaving only ~20° of obliquity within the frontal ~200 km wide fold-belt (Fig. 1). Fold-belt-normal convergence of ~13–17 mm/yr is absorbed by the frontal part of the IBR and has been modeled as elastic loading of the accretionary prism along a locked, east-dipping megathrust with the possibility of a $M_w \geq 8.2$ earthquake (Steckler et al., 2016). Owing to an incomplete paleoseismologic record within the modern GBD, the seismogenic potential of the northern (~22–25°N) segment of the subduction zone remains uncertain. However, an earthquake in 1762 farther south is interpreted as a M_w 8.5–8.8 subduction megathrust event that ruptured northward to 22.5°N (Wang et al., 2013). Although the down-dip end of the locked zone is constrained by GPS data, the structure of the up-dip part of the IBR is not because geodetic data record the present surface elastic deformation field which does not inform the structural geometry.

In this study, we address these uncertainties by focusing on the structure of the frontal part of the Indo-Burman forearc where it rapidly accretes the GBD and partially absorbs highly oblique convergence between India and the Shan Plateau (Steckler et al., 2016). We combine field-mapping, structural analysis, and detrital zircon thermochronology to test for strain-partitioning and determine the structure and geologic shortening rates in the frontal part of the IBR. We find that, despite the high obliquity of convergence, there is only evidence of fold-belt-perpendicular shortening in the frontal fold-belt. Our results emphasize the extent of slip-partitioning across the IBR forearc and inform the regional seismic hazard by documenting the structure of the up-dip part of the accretionary prism.

2. Geologic setting

The frontal fold-belt records ongoing deformation of Paleogene(?)–present Himalayan sourced fluvial-deltaic sedimentary rocks of the GBD (Gani and Alam, 1999; Alam et al., 2003; Najman et al., 2012). GBD sediments on the Indian plate reach to near sea level on the continental shelf and become subaerial at the delta. Teleseismic receiver functions show that the Indian plate has 16–20 km of sediment beneath Bangladesh and northeast India at the latitude of our study area (Mitra et al., 2008, 2018; Singh et al., 2016). Refraction seismic data from the Bengal Fan shows that postrift sediment thickness alone is a minimum of ~13 km near the Bengal delta front (Sibuet et al., 2016).

The frontal ~80 km of the fold-belt is almost entirely buried by ongoing GBD sedimentation, and thus not mapped here, but the locations of the folds are approximated from gas exploration wells and industry reflection seismic data (blind belt in Fig. 1; Sikder and Alam, 2003; Imam and Hussain, 2002; Burgi et al., 2016). Inboard of the blind belt, the outer belt is ~120 km wide and consists of late Miocene–Quaternary fluvial and shallow marine deltaic deposits. The Surma Group within the outer belt consists of Miocene shallow marine shelfal and intertidal deposits. Overlying the Surma Group, the Tipam Group comprises Miocene–Pliocene fluvial deposits including small fluvial distributary channels and large braided river channel deposits. Above that, the Dupi Tila Group consists of Pliocene–Quaternary second-cycle smaller meandering river, floodplain, and alluvial deposits (Figs. 1–3; Alam et al., 2003). Underlying the Surma Group, but not exposed in the outer belt, is the Oligocene Barail Group which includes distal and muddy facies of a lower-shelf to slope or submarine fan depositional environment (Alam et al., 2003).

Within the outer belt, the Surma, Tipam, and Dupi Tila Groups are folded into a series of fault-cored antiforms that define ~10 km wide north-trending ridges. The antiforms are continuous along-strike for tens to >100 km and separated by ~10–20 km wide low relief synclinal valleys (Fig. 2). We define the thrust-front (Fig. 1) to mark the transition from anticlines of the blind-belt with low structural relief and no topographic expression to fault-cored antiforms with topographic relief in the outer belt. In the eastern part of the study area the Barail Group is exposed in the hanging wall of an out-of-sequence reverse fault (Tut Fault, discussed below), we define the boundary between the outer and inner belt at this fault (Figs. 1, 2).

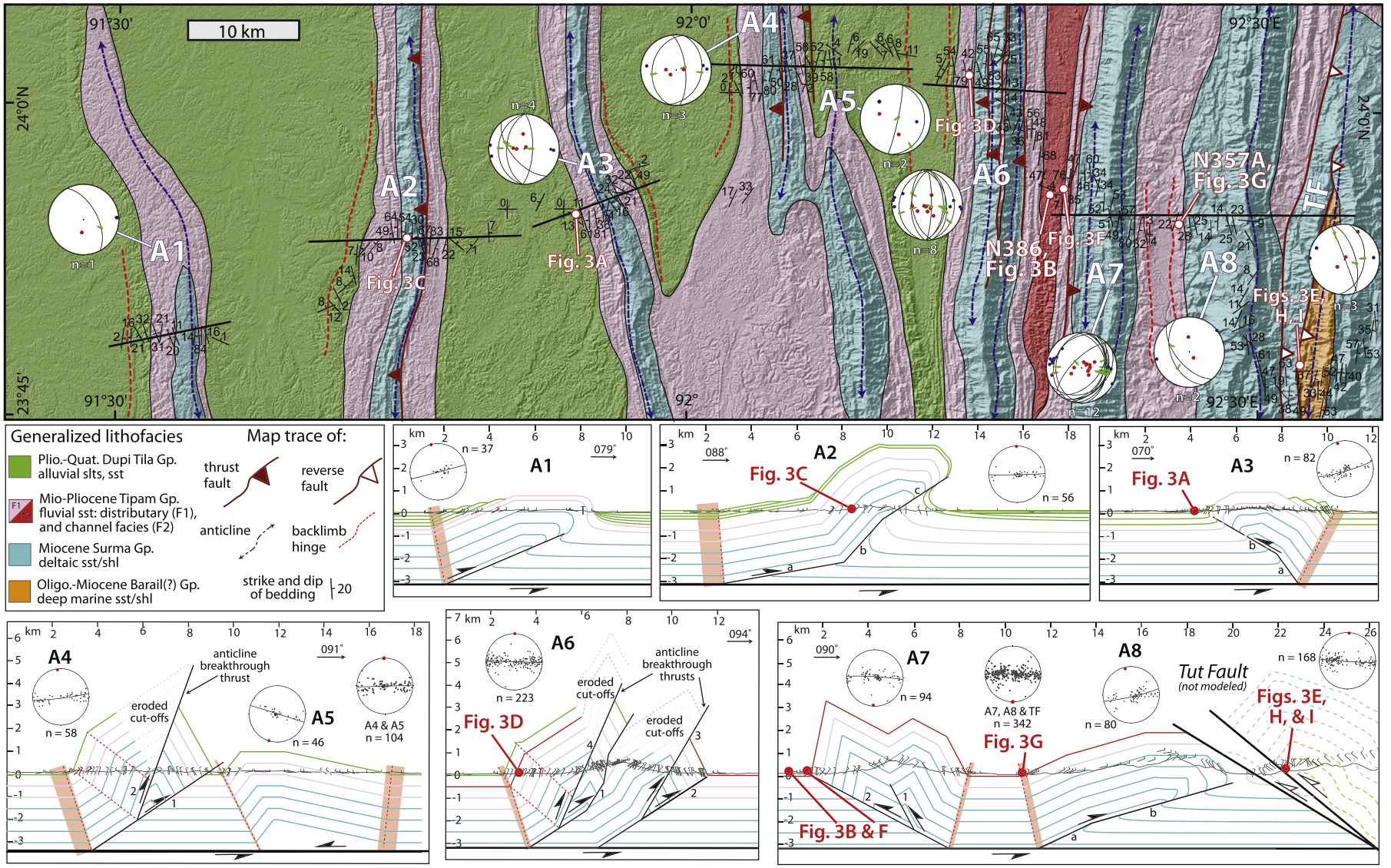

Fig. 2. Geologic map of the study area and cross sections A1–8. Bedding attitudes shown on the map, above, have been reduced to a subset (~15%) of the total data for clarity. The locations of dZFT samples N386 and N357A are shown on the map with red/white circles. See Fig. 1 for locations of dZFT samples MIZ05 and MIZ06 outside of the study area. Stereograms with fault-slip data are shown for each antiform (excluding A2, no data). Black great circles represent fault planes and green arrows show the slip lineation and motion of the hanging wall. Red and blue circles show extension and shortening axes, respectively, for each fault (Marrett and Allmendinger, 1990). All stereograms in this paper are equal area lower hemisphere projections generated with the software *Stereonet* (Cardozo and Allmendinger, 2013). Below, cross sections A1–8 are shown at twice the scale as the map for detail. Small thickness changes in the Tipam and Dupi Tila Groups between sections are based on the map patterns and reflect lateral facies changes. Red shaded rectangles show the permissible location of the back-limb hinge for each antiform that is constrained by surface data which limits the vertical position of the décollement. Stereograms show poles to bedding (black points) with a cylindrical best fit (black great circle) and pi axis (red point) for each antiform. The structure of the Tut Fault (new name and newly mapped) has not been kinematically modeled.

3. Methods

3.1. Geologic mapping

A geologic map of the eight antiforms (A1–8) that define the outer belt in the study area was constructed (Fig. 2). This region is heavily forested so data (bedding dips, $n = 844$) were collected from road-cut outcrops along transects that cross each structural culmination during ~3 months of fieldwork (Fig. 2). Faults and lithologic contacts observed along each transect were extrapolated throughout the study area using a hillshade digital elevation model from the SRTM 1 Arc second (30 m) data (Jet Propulsion Laboratory, NASA).

3.2. Fault and fold kinematic analyses

Fault-slip data ($n = 35$) were collected throughout the study area. Common kinematic indicators including Riedel shears, orientations of associated tensile or sigmoidal veins, and offset bedding (typically ~0.1–10 m of displacement where both fault blocks are preserved) were used to determine the sense of slip. Kinematic axes (incremental shortening, P; and extension, T axes) were calculated for each datum using the software FaultKin. Principal shortening and extension axes for the total fault population in the study area were determined by calculating directional maxima (e1–extension, e2–intermediate, e3–shortening) for clusters of P and T axes using Bingham statistics (Fig. 2, Marrett and Allmendinger, 1990). The orientations of local fold axes for each antiform were determined using a cylindrical best fit to poles to bedding (Fig. 2; total $n = 844$).

3.3. Cross section construction and kinematic modeling

Cross sections A1–8 were constructed perpendicular to the fold axis for each structure (Fig. 2). A combination of forward modeling with the structural geology software MOVE (Midland Valley Exploration Ltd.) and manual cross section construction techniques was used to interpret the kinematic evolution, tectonic shortening magnitudes, and décollement depths for each antiform. Single-ramp trishear and kink-band fault propagation folding, detachment folding, and breakthrough thrusts were constructed using the 2D kinematic modeling algorithms in MOVE (Suppe and Medwedeff, 1990; Hardy and Ford, 1997; and Poblet and McClay, 1996). Imbricate fans of kink-band fault propagation folds were constructed manually. Geologic map data were projected to determine the locations of fault ramps and backlimb axial surfaces of fault-cored folds. The general structural style of each antiform was analyzed to differentiate between trishear or kink-band fault-propagation-folding as well as detachment folding, and to determine the existence (or not) of imbricate or breakthrough faults (Figs. 2–3).

Once a general structural model was determined, the kinematic parameters for each model (e.g., slip, ramp spacing and step-up angle, trishear criteria, décollement depth) were adjusted *ad hoc* until the model limb dips, fold axes, growth strata, faults, and contact locations matched the dip data and geologic map. A goodness of fit was determined by comparing the modeled bedding dips with the measured field data using linear regression analysis. Kinematic parameters were adjusted until only negligible improvements were gained by altering each model. The décollement depth is independently constrained for each structure by the location of the intersection of the backlimb axial surface with the modeled fault. Thus, horizontal uncertainty in the location of the backlimb axial surface determines the vertical uncertainty of the décollement depth (Fig. 2). Shortening that may have been accommodated by volumetric strain or layer parallel shortening was not considered in this analysis so shortening estimates are considered minimums.

3.4. Detrital zircon fission track thermochronology

We applied detrital zircon fission track (dZFT) thermochronology on four samples to determine the maximum depositional age of the fluvial facies in the fold-belt (Tipam Group, sample locations in Figs. 1, 2). The rapidly exhuming Eastern Himalayan syntaxis has provided a source of sediment to the Brahmaputra river with young dZFT ages close to the age of deposition (lag-times of ~2–4 Myr) since at least the middle Miocene (Lang et al., 2016 and references therein). Samples were collected from outcrops of the Tipam Group that have been deformed within the outer belt in order to constrain the maximum age of deformation (Fig. 1). The analytical methods for this dataset are described in supplemental file S3.

4. Results

4.1. Structural analysis of the outer belt

The outer belt near 24°N comprises eight antiforms (A1–8; Figs. 1, 2, 4). The antiforms are generally asymmetric and cored by the Surma Group. Tipam Group deposits crop out on the flanks and sediments of the Dupi Tila Group fill synclines between the structures, onlapping the antiforms (Figs. 2, 3A–D). In some locations antiforms terminate where they overlap (Figs. 1, 2), probably reflecting a strain shadow between the buried ramp segments that core each structure (e.g., A4 and A5, Fig. 2). In the eastern part of the study area, exposures of distal marine shale and fine-grained sandstone deposits are interpreted to be part of the Barail Group. They are uplifted in the hanging wall of a newly mapped, east-dipping reverse fault that we named the Tut Fault, after the Tut River nearby (Figs. 2, 3E, H–I). The Tut Fault juxtaposes the Oligocene(?) Barail Group above the Miocene to Pliocene Surma and Tipam Groups that comprise the outer belt in the footwall (Figs. 2, 3E, H–I). The Tut Fault is the westernmost of several more deeply rooted faults within the inner belt to the east, thus we define the eastern boundary of the outer belt at the Tut Fault.

Within the outer belt, kinematic analysis of faults and folds indicate subhorizontal shortening perpendicular to the northerly structural trend of the fold-belt (Fig. 4B). Of the faults observed ($n = 35$), 33 are thrust faults with slip lineations that have a rake of $>51°$ (e.g., Fig. 3F from the fault tip of A7) and two are oblique, strike-slip faults (from A5, left-reverse; and Tut Fault, right-lateral; Fig. 2). Incremental strain axes determined from fault-slip analyses indicate bulk east-trending subhorizontal shortening and vertical thickening (strain axes e3, and e1, respectively; Figs. 2, 4B) for A1–8 and the Tut Fault. Poles to bedding from A1–8 form generally east–west-striking girdles, cylindrical best fits to the data indicate subhorizontal north–south-trending fold axes for each structure (Figs. 2, 4B). Altogether, the map patterns, bedding dip distributions, and fault-slip data indicate that antiforms in the outer belt accommodate plane strain with generally east–west-trending, subhorizontal shortening axes that are perpendicular to the axial trace of the folds (Figs. 2, 4B).

4.2. Kinematic modeling results

The kinematic modeling results show that the antiforms are asymmetric fault-propagation folds, detachment folds, or imbricate fans of fault-propagation folds with breakthrough thrusts (i.e., Suppe and Medwedeff, 1990) that verge both to the west and east, forming a bivergent fold-thrust belt (Fig. 2). Our distribution of bedding dip data ($n = 844$) reveals that A1–A3, A5, and A8 form relatively simple asymmetric fault-related folds, whereas A4, A6, and A7 contain second-order folds and multiple ramps, indicating more complicated imbricate fan structures. Dupi Tila Group

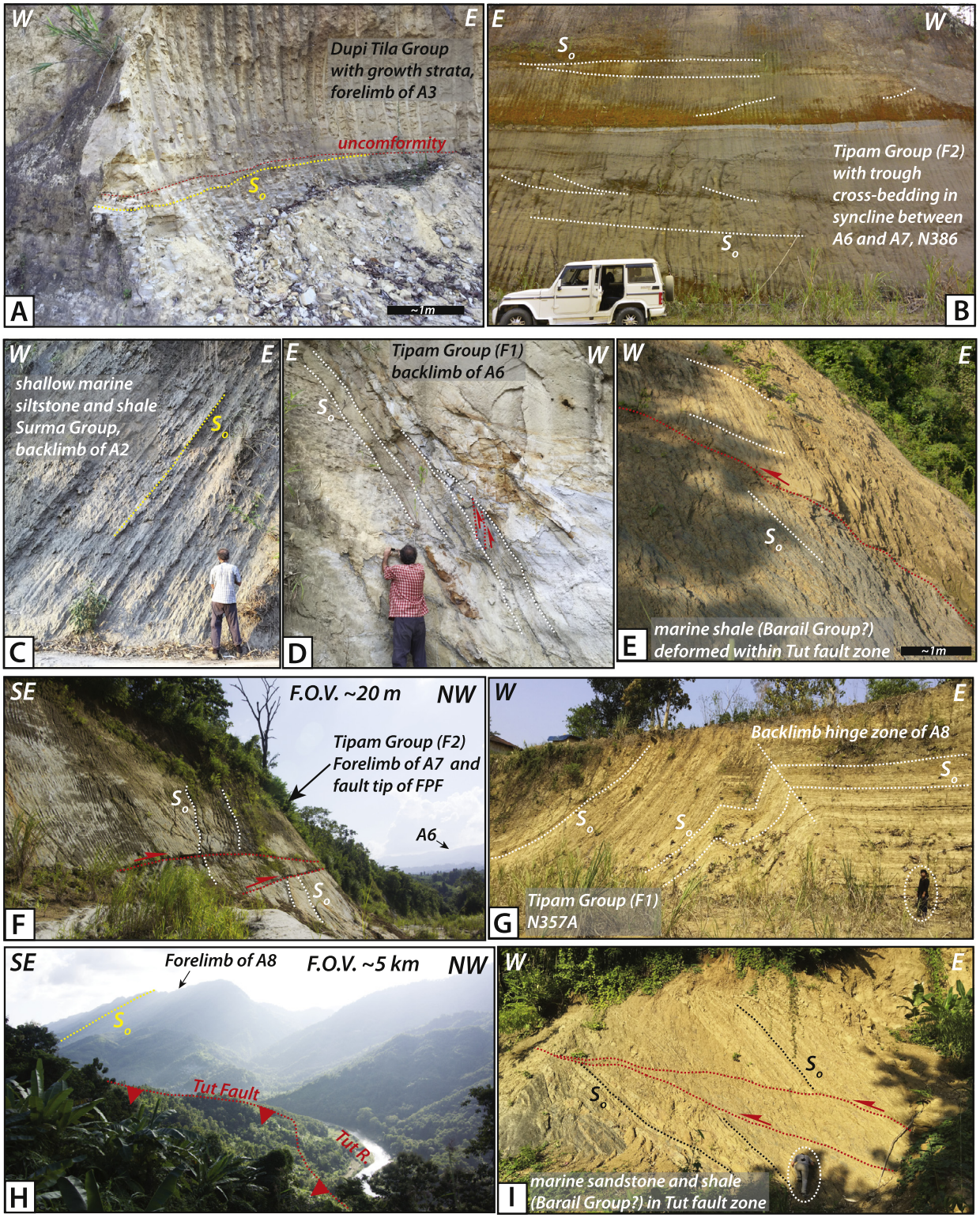

Fig. 3. Field photographs of lithofacies and structures from the outer belt, locations shown in Fig. 2. **A)** Poorly consolidated medium sandstone of the Dupi-Tila group exposed in the forelimb of A3. A local angular unconformity (red line) separates subhorizontal beds (above) from gently tilted (S_0, 143°/08° SW) strata, below, and is interpreted to be a growth strata unconformity. **B)** Poorly consolidated medium-grained sandstone channel deposits of the Tipam Group. White lines show bedding traces (subhorizontal) and >1 m thick, tabular and trough cross-bedding (gently inclined). Sample N386 was collected from this outcrop. **C)** Thinly-bedded (<5 cm thick) shallow marine siltstone and mudstone of the Surma Group containing flaser, lenticular, and wavy bedding as well as low-amplitude (~1 cm) long-wavelength (8–10 cm) ripples. **D)** Steeply-dipping, medium-bedded (white lines), sandstone of the Tipam Group from the backlimb of A6. Minor thrust faults (red lines) record flexural slip that locally thickens a bed within the formation. **E)** Deformed, distal marine shale exposed within the Tut Fault zone. Bedding surfaces dip east (white lines) and are truncated by an east-dipping out of sequence reverse fault (red line). **F)** East-dipping thrust faults (red lines) cut steeply, west-dipping (~60°) beds of the Tipam Group in the forelimb of A7. They are inferred to have formed at the tip of ramp 2 in A7 (Fig. 2). **G)** Mesoscale (tens of meters) kink folds in thinly-bedded (<0.5 m thick) sandstone deposits of the Tipam Group within the back-limb hinge zone of A8 (Fig. 2). Sample 357A was collected from this outcrop. **H)** View southwest of the mapped trace of the Tut Fault near the Tut River. In the background, strata of the Surma Group dip east on the forelimb of A8 (yellow line). **I)** Deformed distal marine shale and interbedded sandstone deposits (Barail Group) within the Tut fault zone (near E and H). Bedding (black lines) is truncated by several east-dipping thrust faults.

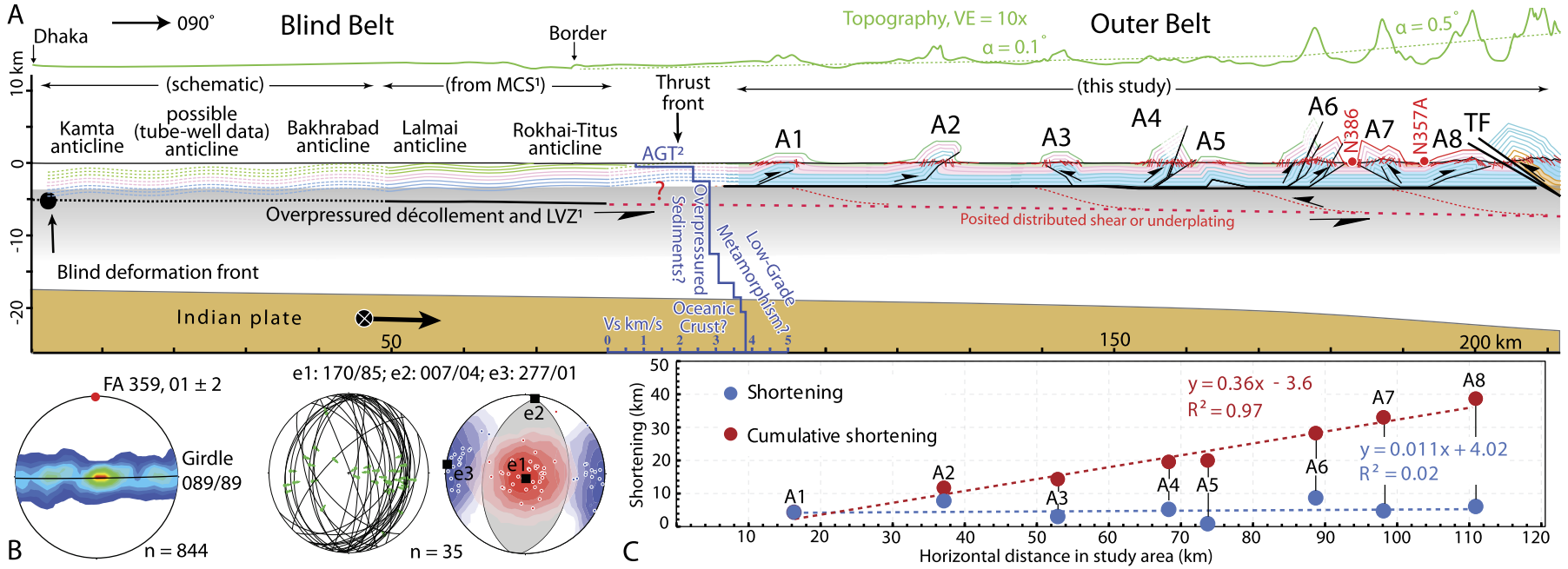

Fig. 4. A) Cross section of the outer and blind belts (no vertical exaggeration; location in Fig. 1). The Lalmai and Rokhai-Titus anticlines and low-velocity zone (LVZ) are after seismic data (Ref. 1, Sikder and Alam, 2003). The Kamta, Bakhrabad and 'possible anticline' are not constrained but inferred from the locations of gas fields (Fig. 1). Red circles show locations of dZFT samples. Faults indicated with red dashed lines show posited distributed deformation within or below the décollement horizon and are not constrained. Blue curve labeled AGT shows shear wave velocities with depth from teleseismic receiver functions from a station in the city of Agartala (Ref. 2, Fig. 7 of Mitra et al., 2008), the vertical scale is the same as the cross section and the velocity scale is given in blue text at the base. The green curve, above, shows topography with 10× vertical exaggeration, α–mean surface slope (dashed green line). **B)** Stereograms showing: left, Kamb contours (contour interval = 2σ) of poles to bedding with cylindrical best fit (girdle, great circle) and regional fold axis (FA, red circle); middle, flexural slip and thrust faults (great circles) and striations (green arrows), arrows show sense of motion of the hanging wall; right, incremental shortening (blue) and extension (red) axes from the faults, contour interval = 2σ. The principal strain axes of the population (e1–extension, e2–intermediate, and e3–shortening) are shown with black squares. **C)** Graph showing shortening (blue) and cumulative shortening (red) magnitudes for each antiform A1–8 with linear best fits, horizontal scale is the same as in A.

Table 1
Kinematic modeling criteria for antiforms A1–8.

	Structure type	Shortening (km)	Décollement depth (km)	Footwall cut-off/step-up angle (deg.)	Trishear p/s ratio	Trishear angle; offset	Forelimb dip (deg.)	Backlimb dip(s) (deg.)	m^*	R^2
A1	Trishear FPF	3.8	3.1 ± 0.11	23	1.5	50; 0.5	–	23	0.93	0.93
A2	Trishear FPF	7.6	3.1 ± 0.06	a) 10; b) 48; c) 33	1.5	50; 0.5	–	10, 48	1.19	0.93
A3	Trishear FPF	2.8	3.1 ± 0.29	a) 54; b) 30	a) 1.8; b) 1.7	50; 0.6	–	54, 30	0.95	0.92
A4	Kink band FPF w/ breakthrough thrust	4.9	3.4 ± 0.28	1) 34; 2) 36	–	–	61	34, 70	0.94	0.93
A5	Detachment fold	0.6	3.4 ± 0.09	–	–	–	52	12	1.08	0.85
A6	Imbricate fan: 2 kink band FPFs w/breakthrough thrusts	8.4	3.2 ± 0.09	1) 33; 2) 33; 3) 27; 4) 33	–	–	63	66, 33	0.99	0.86
A7	Imbricate fan: 2 kink band FPFs	4.5	3.2 ± 0.06	1) 34; 2) 28	–	–	78	62	0.93	0.92
A8	Trishear FPF	5.8 Total 38.4	3.2 ± 0.08	a) 25; b) 16	a) 1.2; b) 1.8	50; 0.5	–	25, 16 Average	1.08 1.01	0.90 0.91

* m = slope of regression line between modeled and observed dips.

deposits were observed onlapping the flanks of A1–3 and were modeled as growth strata (Figs. 2, 3A). All of the model results have an R^2 value between 0.85 and 0.93 and the best fit slopes (m) of the correlation of the observed and modeled dips scatter around a value of 1 ($0.93 \leq m \leq 1.19$; Table 1). Values of $R^2 = 1$ and $m = 1$ would indicate a perfect fit. The kinematic models for each structure (Fig. 2) are described here and summarized in Table 1.

Anticline 1 is an east-vergent fold, cored by a blind fault, with a homoclinally west-dipping (23°) backlimb, flat top, and subvertical east-facing forelimb. A1 is modeled as a trishear fault-propagation fold with a single 23° west-dipping ramp. Projecting the back-limb axial surface to the ramp constrains the décollement depth to 3.1 ± 0.11 km. The dip data and lithologic contacts on either side of the fold limit the amount of slip to ∼3.8 km.

Anticline 2 is also an east-vergent structure with a subvertical to gently overturned east-facing forelimb. The backlimb has three segments of different dip and the ramp juxtaposes Surma Group in the hanging wall (Fig. 3C) above the Tipam Group. The best fit model for this structure is a trishear fault-propagation fold over a single ramp with two bends that match the change in bedding dips on the backlimb. The projected décollement depth is 3.1 ± 0.06 km. Lithologic contacts, the stratigraphic separation across the fault, and the shape forelimb limit the slip to ∼7.6 km.

Anticline 3 verges west and is characterized by a subvertical west-facing forelimb, flat top, and moderately (30°) to steeply (60°) dipping backlimb. The curved forelimb and change in dip of the backlimb was fit with a trishear fault-propagation fold model using an east-vergent ramp with a fault bend between steep (54° dip) and gently (30°) dipping segments. The location of the backlimb hinge requires a 3.1 ± 0.29 km deep décollement. Growth strata and the shape of the forelimb limit the amount of slip to ∼2.8 km.

Anticline 4 is characterized by a gently (34°) to steeply (70°) west-dipping backlimb and a steeply east-dipping (61°) forelimb. In contrast to A1–3, the anticline crest of A4 is a kink-fold with planar limbs. Thus, the forelimb of A4 is modeled with an east-verging kink-band fault propagation fold over a single east-dipping ramp (34°, ramp 1). The steeply dipping (70°) backlimb requires an additional ramp to cut out the anticlinal hinge, forming an anticline breakthrough thrust (ramp 2). The breakthrough thrust is modeled with a step-up angle of 36° to produce the change in dip of the backlimb from 34° to 70°. Although the hanging-wall cutoffs of ramp 2 are eroded, the location of the axial surfaces (red dashed lines) between the steeply and gently dipping parts of the backlimb limit the slip on ramp 2 to ∼1.8 km. Projecting the backlimb axial surface to ramp 1 limits the detachment depth to 3.4 ± 0.28 km. The total shortening for A4 is ∼4.9 km.

Anticline 5 verges west and is characterized by a steeply dipping (52°) forelimb, flat top, and a gently dipping backlimb (12°). A5 was most accurately modeled as an asymmetric detachment fold with constant limb dips. Kink-band or trishear fault-propagation fold models predict an overturned or substantially thickened forelimb for the gently-dipping ramp required to match the backlimb, and thus, did not produce an acceptable fit. The dip data constraining the location axial surfaces predict a 3.4 ± 0.09 km deep detachment. The shortening for A5 is ∼0.6 km.

Anticline 6 is characterized by a steeply to moderately west-dipping backlimb (66° to 33°, Fig. 3D) and steeply east-dipping forelimb (63°) that are separated by several second order ramps and narrow kink-folds. The east-facing forelimb is modeled as a kink-band fault propagation fold over a west-dipping ramp (33°, ramp 2). To model juxtaposition of Surma Group deposits over Tipam Group deposits and tight folding and near the crest of the structure, a blind ramp (ramp 1, initial dip of 33°) is inferred to have been translated over ramp 4, forming an imbricate fan. Between ramps 1 and 2, Surma Group deposits again crop out structurally above the Tipam Group. Thus, an anticline breakthrough thrust (ramp 3) with a step-up angle of 27° is inferred to cut through the forelimb of ramp 2, uplifting the Surma Group. Although ramp 3 does not crop out, several minor thrust surfaces were observed nearby, prompting our interpretation of a breakthrough fault in this location. The west-facing backlimb of A6 was also modeled with an anticline breakthrough thrust (ramp 4) that cuts through the forelimb of ramp 1 with a step-up angle of 33°. This geometry satisfies the requirement of steeply dipping (66°) Tipam and Surma deposits on the backlimb. Although the hanging wall cutoffs of ramps 3 and 4 are eroded, the locations of the hinges separating differently dipping segments of the backlimbs (red dashed lines), as well as the location of the contact between the Tipam and Surma Groups, limits the slip to ∼1.1 km for ramp 3 and ∼1.7 km for ramp 4.

Altogether, our interpretation of A6 requires an imbricate fan of two east-vergent kink-band fault propagation folds (ramps 1, 2) that each develop an anticline breakthrough thrust (ramps 3, 4). The projection of the backlimb axial surface of ramp 1 predicts a 3.2 ± 0.1 km deep décollement horizon. The position and shape of the forelimb, as well as the geometry of the secondary structures in the core of the antiform, limits the cumulative slip of the ramps 1–4 to ∼8.4 km. The topographic expression of A6 diverges to the north of the study area, forming two antiformal structures with lower relief (Fig. 1). Thus, the more complex structure of A6 may record the superimposition of two anticlines formed by ramps 1

and 4 and by ramps 2 and 3 that were initially separated by a narrow syncline.

Anticline 7 verges west and is characterized by a steeply west-dipping forelimb (~78°) and two second-order, west-verging anticlines with narrow hinges that uplift and fold the Surma Group. The backlimb dips steeply east (~57°). To match the steep forelimb and backlimb, as well as the second order closed folds, A7 is modeled as an imbricate fan of two west-vergent kink-band fault propagation folds. Several minor thrusts that imbricate fluvial deposits of the Tipam Group crop out within the forelimb hinge above the fault tip of the lower ramp (ramp 2; Fig. 3F). The location of the backlimb hinge is constrained by an array of kink-bands with steeply west-dipping axial planar cleavage that deform the Tipam Group. The projection of the backlimb axial surface to the intersection with ramp 2 predicts a 3.2 ± 0.06 km deep décollement. The geometry of the forelimb and the two second-order anticlines limits the cumulative slip on both ramps to ~4.5 km.

Anticline 8 is defined by a moderately west-dipping backlimb (16–25°, Fig. 2), a flat top, and a steeply-dipping, east-facing forelimb. The anticline crest of A8 is curved, and thus, A8 is modeled as an east-vergent trishear fault-propagation fold over a single ramp with two segments that match the change in dip of the backlimb (25–16°). The projection of the backlimb axial surface (Fig. 3G) predicts a décollement depth of 3.2 ± 0.08 km and the geometry of the forelimb limits the total slip to ~5.8 km. East of anticline 8, the more deeply rooted Tut Fault dips east and uplifts the Barail Group above the Surma and Tipam Groups in the footwall, indicating that it is an out-of-sequence fault that cuts the décollement of the outer belt (Figs. 2, 3E, H–I).

The kinematic models predict a decollement depth that ranges between ~3.1 to ~3.4 km below sea level with a maximum vertical error of ±0.3 km (Fig. 2, Table 1). A composite cross section was constructed by projecting A1–8 into an east–west striking profile parallel to the bulk transport direction determined from kinematic analysis of the folds and minor faults (Fig. 4). Shortening magnitudes for A1–8 range between 0.6–8.4 km and depend on where the section line crosses each structure (Fig. 4C, Table 1). Hence, there is no systematic trend in shortening magnitude per antiform with distance from the deformation front. However, cumulative shortening shows a linear increase with horizontal distance across the study area (Fig. 4C). Altogether, the eight antiforms that define the outer belt accommodate ~38.4 km of shortening above a ~3.1–3.4 km deep, subhorizontal décollement. A maximum uncertainty in shortening ±16 km was determined using an area balance estimation. Area-balancing is independent of any particular kinematic model, and thus, encompasses a range of viable alternative interpretations (supplemental file S1A; Judge and Allmendinger, 2011). A viable step-wise reconstruction of the outer belt is presented in supplemental file S1B.

Our kinematic modeling employs classical fault-propagation fold theory which assumes beds of constant thickness are pushed over a ramp that propagates up from a planar detachment. It is also possible that the décollement horizon has a finite thickness and accommodates shear or that the fault ramps are break-thrusts that cut through existing gentle detachment folds. Shear fault-bend fold theory or wedge-thrust fault-bend fold theory with footwall shear (Mueller and Suppe, 1997; Suppe et al., 2004) could also be used to model the backlimb kinematics of some of the structures (A1–3, A8). Any of these possibilities could predict a deeper base of deformation depending on the thickness of the décollement. Because it is impossible to know the décollement horizon thickness, shear angle, type of shear, and possibility of heterogeneously distributed shear from surface data alone, a quantitative investigation of shear fault-bend folds or break-thrusts cannot be carried out without seismic images (Suppe et al., 2004). Although shear fault-bend folding could be used to model some of the structures,

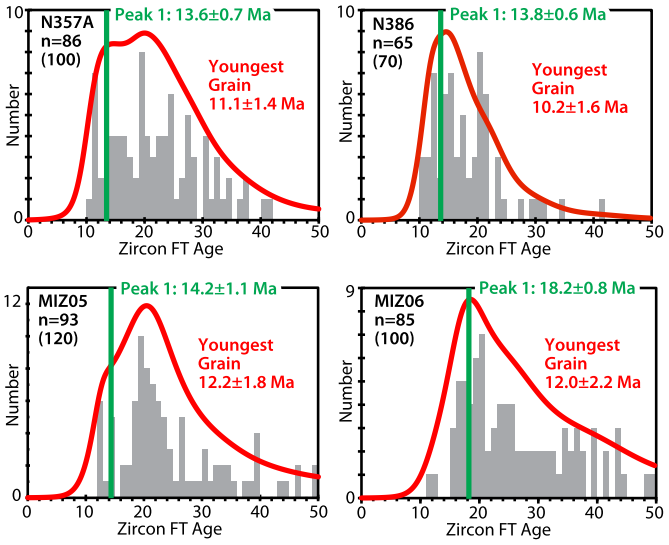

Fig. 5. Histograms and probability density functions (red curve) showing detrital zircon fission track results for samples N386, N357A, MIZ05 and MIZ06. The youngest peak age is given with a green bar. Youngest single-grain ages and errors are listed in red text and used to determine maximum depositional ages.

we found that other structures (i.e., A4, A6, A7) cannot be readily modeled from a detachment that is deeper than 3.1–3.4 km. Our constant thickness projections limit the top of the detachment horizon to 3.1–3.4 km, however, its true thickness cannot be precisely constrained by our data. One published but poor-resolution industry seismic line collected near our profile on A1 shows the base of folding near the bottom of the image at ~2.3 s TWTT (supplemental file S2). This is equivalent to ~3.1 km using unpublished velocity data from the Titus well nearby (Fig. 1), a good match to our result. To account for the possibility of a sheared décollement of finite thickness as well as honor the surface geologic constraints from this study and the limited available subsurface data, we suggest qualitatively extending the lower limit for the detachment horizon to ~4 km below sea level.

4.3. Detrital thermochronology results

In four dZFT samples from deformed fluvial deposits of the Tipam Group, the youngest single grain ages are between ~12–10 Ma (Fig. 5). Considering a minimum lag-time of ~2 Ma (Lang et al., 2016 and references therein) implies a maximum depositional age of ~8 Ma, limiting the onset of deformation in the outer belt to ≤8 Ma. From our outer belt shortening estimate of 38.4 ± 16 km, this equates to a shortening rate of ≥4.8 ± 2.0 km/Myr. Given that active fluvial sedimentation is currently occurring over the blind belt (Fig. 1), Tipam Group fluvial sedimentation in the outer belt likely only ceased with uplift related to westward propagation of the thrust front. Sample N357A is currently ~120 km east of the thrust front (Figs. 1, 4), indicating a thrust front propagation rate of ≥15 km/Myr. The rate of underthrusting of an orogenic wedge equals its shortening rate (4.8 km/Myr for the outer belt) plus the propagation rate (≥15 km/Myr) of the wedge (DeCelles and DeCelles, 2001), giving an underthrusting rate of ≥19.8 km/Myr for incoming sediments in the lower plate below the décollement. These timing constraints indicate that the IBR has the fastest known growth rate for an active accretionary prism worldwide (Kastens, 1991). Considering a longer dZFT lag time that may be more representative of frontal Himalayan erosion (~4 Ma, Lang et al., 2016), rather than the accelerated erosion rates of the Eastern Himalayan syntaxis, increases the shortening and propagation rates to 6.4 ± 2.7 km/Myr and >20 km/Myr, respectively.

5. Discussion

5.1. Weak regional décollement, structural style and kinematics of the outer belt

The shallow, subhorizontal décollement and simple geometry of the synclines between each antiform constrained by our analyses are consistent with previous interpretations of reflection seismic and well data from Bangladesh. Our projected décollement depth of ~3.1–3.4 km corresponds with a 3–5 km deep overpressured horizon (≥92% of lithostatic pressure) identified in sonic log data from wells in the outer and blind belts (Zahid and Uddin, 2005; Steckler et al., 2008). A décollement horizon was also interpreted at a 3.1 km deep contact between the Surma and Barail Groups in a core taken from an anticline in the outer belt south of the study area (Sitakund 1 well, Fig. 1; Sikder and Alam, 2003). This is consistent with our observation that the Barail Group crops out in the hanging wall of the more deeply rooted Tut Fault but not in any of the fault-cored antiforms within the outer belt, indicating that the décollement is located at the stratigraphic contact between the Barail and Surma Groups. We deduce that overpressure at and below the transition between well-indurated sandy shallow marine and intertidal deposits (upper Surma Group) and underlying fine-grained deeper water deposits (Barail and lower Surma Group) controls the stratigraphic level of the décollement (Sikder and Alam, 2003). Altogether, our findings indicate that the outer belt is a thin-skinned fold-thrust belt that reflects ongoing accretion of GBD sediment above a 3.1–3.4 km deep décollement (Fig. 4; cf., Gani and Alam, 1999).

To the west and south of the study area, the décollement horizon was mapped onshore at ~3.0–3.5 s TWTT on industry reflection seismic profiles (Sikder and Alam, 2003; Maurin and Rangin, 2009). Using velocity data from wells in Bangladesh (unpublished industry data) we estimate that this corresponds to a depth of ~5–6 km, ~2–3 km deeper than the Sitakund 1 core and our results for the outer belt. We infer that the 3.1–3.4 km décollement in our study area is laterally continuous with the structures documented in reflection seismic, core, and well data but is up to ~3 km shallower in the outer belt than in the blind belt. Comparing our result with this previous work indicates there is both along- and across-strike topography of the décollement (Burgi et al., 2016). Contributions to the lateral changes in décollement depth include the subsidence of the Sylhet basin by the flexural load of the Shillong massif to the north (Fig. 1; Najman et al., 2016) as well as ongoing subsidence and sediment loading of the delta and blind belt to the west and south (Grall et al., 2018). We further propose that distributed shear within a thick décollement horizon and/or subdécollement structural thickening (i.e., underplating) may contribute to the apparent uplift of the outer belt relative to the blind belt. Sediment underplating has been documented at subduction margins worldwide, for example: Makran (Kopp et al., 2000) and Nankai (Park et al., 2002). Although poorly constrained, if this underplating hypothesis is correct, then the possibility of deeper structures beneath the outer and inner belts impacts the regional seismic hazard (Fig. 6).

The morphology of the outer belt that is characterized by an extremely low surface slope (0.1°, Steckler et al., 2008) and laterally continuous, overlapping, bivergent antiforms yields some information about the strength of the shallow décollement. The low slope and overpressured shale décollement place the IBR in a class of critical wedges characterized by extremely high basal pore-fluid pressures (Bilotti and Shaw, 2005) resulting in low effective friction along the décollement. Solving the critical taper equations of Davis et al. (1983) requires an effective basal friction angle of <1° (equivalent to >95% overpressure) to account for the mean surface slope of the outer belt (0.1°). This matches the measured

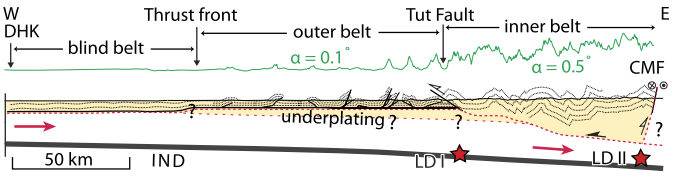

Fig. 6. Schematic cross section of the IBR between the deformation front and the CMF. Blind and outer belts are shown in Fig. 4. Posited subdécollement structures are shown with red-dashed lines. The structure of the inner belt is projected from our unpublished surface data but not modeled here. Red arrows give the motion of lower plate. The green line shows topography with a vertical exaggeration of 10x. Abbreviations: CMF – Churachandpur-Mao Fault; DHK – city of Dhaka; IND – Indian plate; LD I and LD II – locking depths I and II after Steckler et al. (2016).

overpressure from wells in the outer belt (92–97% of lithostatic, Zahid and Uddin, 2005; Steckler et al., 2008). Moreover, bivergent antiforms that overlap and/or change vergence along strike occur in low-taper fold-thrust belts defined by weak, shallowly-dipping decollements such as the Niger Delta toe (Bilotti and Shaw, 2005; Higgins et al., 2009). In the IBR, the displacement to length ratio for the antiforms is low ($\sim 10^{-2}$) indicating low rock shear strength for the upper plate (Cowie and Scholz, 1992). These morphological observations are consistent with critical taper theory for a weak fold-belt sliding above a décollement of very low effective friction.

Our structural data and kinematic analyses demonstrate that the outer belt reflects plane-strain with subhorizontal, east-trending shortening that is normal to the axial trace of the fault-cored folds (Figs. 1, 2, 4). In contrast to some previous kinematic interpretations of the IBR (Maurin and Rangin, 2009), we found no evidence of significant dextral shear in the outer belt. South of ~23.5°N, the trend of fold-belt curves to the south–southeast where the GPS vectors are sub-perpendicular to the structural trend (Fig. 1), and thus, we contend that there is little reason to infer right-lateral, basement involved faulting within the outer belt. There are a few ($n = 4$) shallow (<30 km) thrust-fault focal mechanisms within the outer belt and just one strike-slip focal mechanism at the boundary with the inner belt (Global CMT catalog; Steckler et al., 2008; Rangin et al., 2013; Wang et al., 2014). Our results are consistent with these shallow thrust events, some including surface breaks, and indicate that east-trending shortening of the upper plate is kinematically decoupled from strike-slip and normal faulting within the underlying subducting crust that is illuminated by intermediate depth (30–100 km) seismicity (i.e., Rangin et al., 2013). Our results are also consistent with the map of active structures of Wang et al. (2014), who found no geomorphologic evidence for strike-slip faulting in the outer belt. Furthermore, our geologic mapping revealed no evidence of significant normal faulting within the fold belt, precluding interpretations that gravity collapse features at the shelf break are driven by hinterland extension of the IBR (Rangin, 2017). Instead, our results indicate that the eastward component of the oblique plate convergence is partitioned to the up-dip part of the IBR, including the blind and outer belts.

The discrepancy between the oblique (~20° obliquity; Fig. 1) GPS vectors in the outer belt and the geologic shortening axes normal to the structural trend of the fold-belt can be accounted for by strain-partitioning. GPS vectors record the present elastic deformation field associated with oblique slip on the megathrust down-dip below the locking depth (Steckler et al., 2016), and thus, do not provide any information constraining the up-dip structure of the IBR. However, our structural analyses (Fig. 2) indicate nearly full strain partitioning of the frontal part of the IBR such that the outer and blind belts absorb the component of plate motion that is normal to the structural trend (Nielson et al., 2004; Steckler et al., 2016). Most fold-belt parallel motion is taken up

along north-striking dextral faults in the internal part of the IBR (i.e., SF and CMF; Steckler et al., 2016) as has been observed at other oblique subduction zones (McCaffery et al., 2000; Bradley et al., 2017). Thus, the observed obliquity of geodetic vectors in the outer and blind belts reflects accumulation of interseismic elastic strain down-dip below the locking depth, which may or may not match the slip vectors of megathrust earthquakes, and does not match the principal strain axes, documented herein, from cumulative deformation of the upper plate (cf. Bradley et al., 2017). The structural trend of accretionary wedge fold-thrust belts is usually trench parallel even when subduction is oblique (e.g., McCaffrey et al., 2000). Hence, our results indicate that the frontal part of the IBR is a nearly fully partitioned accretionary wedge that absorbs the fold-belt normal component of India–Shan motion (cf., Nielsen et al., 2004; Steckler et al., 2016) above a weak, shallow megathrust.

5.2. Deformation rates and implications for active faults

Our thermochronology results and shortening estimate of ∼38.4 km across the outer belt indicate a minimum geologic shortening rate of ≥4.8 mm/yr, at least 28–37% of the total fold-belt-normal component of the geodetic convergence rate across the IBR (∼13–17 mm/y; Steckler et al., 2016). Assuming the short-term geodetic rate matches the long-term rate requires that there has been ≥104–136 km of convergence across the accretionary prism since ∼8 Ma. Buried anticlines in the blind belt are open folds that do not take up much shortening (Fig. 1, 2; Sikder and Alam, 2003). Even considering layer-parallel shortening by sediment compaction (∼20–40% volume loss; Saito and Goldberg, 2001), shortening taken up by the blind and outer belts is insufficient to account for all of the expected plate convergence. The remaining convergence must therefore be absorbed within the internal part of the IBR, including the Tut Fault and CMF (Figs. 1, 4; Wang et al., 2014). This implies that shortening has been distributed across the blind, outer, and inner belts since the late Miocene. Posited subdécollement structure may also absorb shortening that is not accounted for here.

Maurin and Rangin (2009) report a ∼2 Ma age for deformation of the frontal part of the IBR based on the age of a latest Pliocene marker bed that onlaps an anticline in the blind belt offshore. Their result is roughly consistent with our maximum age for deformation of ∼8 Ma from antiforms A7 and A8 and our estimated westward propagation rate of ≥15 km/Myr, by ∼2 Ma deformation should have propagated westward to the blind belt. The linear increase in cumulative shortening of the outer belt with distance from the deformation front (Fig. 4C) indicates a uniform décollement slip-rate for the outer belt (Chapman and Williams, 1984) and suggests that shortening was concentrated at the frontal structure in a series of forward-propagating ramps (Hardy et al., 1998). This pattern is also consistent with the rapid (≥15 km/Myr) rate of forward propagation of the thrust front and spatially correlates with the modeled locked area of the megathrust (Steckler et al., 2016), suggesting that a rupture may propagate to the frontal structure either at the thrust front along the ∼3.1–3.4 km décollement or the blind deformation front along a deeper (∼5–6 km) décollement (Figs. 1, 4).

The uniquely large size of the IBR is an important trait pertinent to its structure when compared with most other subduction zones. The maximum incoming sediment thickness to active accretionary prism width ratio for the IBR is ∼20:375 (in km). For comparison, northern Sumatra is ∼2:70; Nankai is ∼1:30; and Makran is ∼7:200 (Kopp et al., 2000; Hubbard et al., 2015). These comparisons indicate that despite the IBR's large size, its thickness to width ratio is similar to other accretionary prisms (∼1:20–1:30). Our findings show the outer belt advanced rapidly (>15 km/Myr) westward after the late-Miocene and coincident with Pliocene avulsion of the Brahmaputra River around the Shillong Massif and arrival of the modern GBD (Najman et al., 2016 and references therein). We propose that the high sedimentation rate in the GBD likely contributed to the development of overpressure in the basin which led to weakening of the decollement and consequent rapid westward expansion of the outer belt necessary to maintain its sediment thickness to width ratio and critical taper angle. The remaining ∼13–17 km thick section of rapidly (≥20 km/Myr) underthrust sediment on the Indian plate must be either subducted or accreted by underplating to the internal part of the wedge.

Despite being subaerial, the IBR shares important characteristics of submarine subduction accretion systems that have generated large coseismic displacements on the up-dip part of the megathrust during a great earthquake, including slip partitioning and the existence of a shallow, weak and overpressured décollement (Lay et al., 2012; Kimura et al., 2012). For example, tens of meters of shallow coseismic displacements occurred during the 2011 Tohuko M_w 9.0 rupture (Sun et al., 2017) and the 2004 M_w 9.2 Sumatra earthquake (Ammon et al., 2005). These events demonstrated that large ruptures can occur along the up-dip parts of accretionary prisms even if they are weak and occur in a stress shadow of a locked segment down-dip (Almeida et al., 2018) or at an oblique convergent margin. Furthermore, the largest subduction earthquakes are thought to preferentially occur at subduction zones with thick accumulations (>1 km) of incoming sediment (Scholl et al., 2015).

GPS data suggest the frontal part of the IBR is coupled and elastically loading (Steckler et al., 2016), despite being overpressured and weak. However, geodetic coupling does not inform the mechanical properties of the shallow décollement (Almeida et al., 2018). Although the IBR has the potential for a large, shallow (∼3–4 km deep) coseismic rupture, the likelihood of such an event also depends on the frictional properties of the décollement (i.e., velocity weakening or strengthening, Scholz, 1998). For example, a 1762 event off the Chittagong and Arakan coast has been interpreted as a megathrust event of M_w 8.5–8.8 (Wang et al., 2013) on the next segment of the plate boundary to the south. However, models of this event suggest that the rupture did not progress all the way to the deformation front (Wang et al., 2013; Mondal et al., 2018). Wang et al. (2014) suggest several possible scenarios for megathrust ruptures in the IBR where individual earthquakes may either rupture to thrust front or the deformation front. Ongoing evaluation of the regional seismic hazard should consider the shallow décollement documented herein as well as its lateral extent and regional structural relief. Future investigations could be undertaken to evaluate the coseismic frictional properties of the décollement horizon.

6. Conclusions

The 120 km wide outer belt of the IBR is detached along a shallow (∼3.1–3.4 km deep) décollement that formed in an overpressured shale horizon of unknown thickness. Fault-cored antiforms in the outer belt record plane strain with principal shortening axes normal to the axial traces of the folds. Upper plate east–west shortening of 38.4 ± 16 km has been absorbed across the outer belt above the shallow décollement since ∼8 Ma, indicating a minimum shortening rate of ∼4.8 mm/yr, a thrust front propagation rate of ≥15 km/Myr, and a sediment underthrusting rate of ≥20 km/Myr. The geologic shortening rate of the outer belt is at least 28–37% of the fold-belt normal component of the geodetic convergence rate across the IBR.

Critical taper theory and the bivergent structural style of the outer belt indicate a weak stratigraphic section that is sliding along

a décollement of very low effective strength. The shallow, weak décollement is the up-dip part of a megathrust that has the potential to accommodate large coseismic slip during a great ($\geq M_w$ 8) earthquake. A change in the décollement depth between the blind and outer belts (thrust front) is interpreted to record a combination of flexural subsidence related to the Shillong Massif to the north, ongoing subsidence of the GBD to the west, and posited subdécollement structural thickening below the outer belt.

Our results indicate that the IBR forearc is an active subduction boundary characterized by nearly full slip-partitioning. The outer belt only absorbs the fold-belt normal component of India–Shan motion. Therefore, the fold-belt parallel component must be partitioned among strike-slip faults in the internal part of the IBR, including the Churachandpur–Mao and Sagaing Faults. Whether the young, nascent part of the IBR would rupture seismically to the thrust front or to the blind deformation front remains an open question of critical importance to the regional seismic hazard and the megacity of Dhaka which lies astride the deformation front.

Acknowledgements

This project was supported by NSF OISE 09-68354 and EAR 17-14892. We would like to thank Vineet Gahalaut from the National Centre for Seismology, Delhi for his collaborative support for this project. We also thank Rafael Almeida and Judith Hubbard from the Earth Observatory of Singapore, as well as Paula Burgi from Cornell, for several productive discussions about this work. We are grateful to Victor Ralte, Paul Lalnuntluanga, J. Malsawma, and C. Lalremruatfela from Mizoram University and Government Zitiri Residential Science College for introducing us to the geology of Mizoram and Tripura. Comments from two anonymous reviewers improved this manuscript. We dedicate this paper in memory of Victor Ralte.

Appendix A. Supplementary material

Supplementary material related to this article can be found online at https://doi.org/10.1016/j.epsl.2018.09.003.

References

Alam, M., Alam, M.M., Curray, J.R., Chowdhury, M.L.R., Gani, M.R., 2003. An overview of the sedimentary geology of the Bengal Basin in relation to the regional tectonic framework and basin-fill history. Sediment. Geol. 155 (3–4), 179–208. https://doi.org/10.1016/S0037-0738(02)00180-X.

Almeida, R., Lindsey, E.O., Bradley, K., Hubbard, J., Mallick, R., Hill, E.M., 2018. Can the up-dip limit of frictional locking on megathrusts be detected geodetically? Quantifying the effect of stress shadows on near-trench coupling. Geophys. Res. Lett. http://doi.org/10.1029/2018GL077785.

Ammon, C.J., Ji, C., Thio, H., Robinson, D., Ni, S., Hjorleifsdottir, V., et al., 2005. Rupture process of the 2004 Sumatra–Andaman Earthquake. Science 308, 1133–1139. https://doi.org/10.1126/science.1112260.

Bilotti, F., Shaw, J.H., 2005. Deep-water Niger Delta fold and thrust belt modeled as a critical-taper wedge: the influence of elevated basal fluid pressure on structural styles. Am. Assoc. Pet. Geol. Bull. 89 (11), 1475–1491. http://doi.org/10.1306/06130505002.

Bradley, K.E., Feng, L., Hill, E.M., Natawidjaja, D.H., Sieh, K., 2017. Implications of the diffuse deformation of the Indian Ocean lithosphere for slip partitioning of oblique plate convergence in Sumatra. J. Geophys. Res., Solid Earth 122 (1), 572–591. http://doi.org/10.1002/2016JB013549.

Burgi, P. Hubbar, J. Peterson, D.E. Akhter, S.H., 2016. Fault Geometry Beneath the Chittagong–Myanmar Fold and Thrust Belt, Bangladesh, and Implications for Earthquake Hazard. Abstract T13D-03 presented at 2016 Fall Meeting, AGU, San Francisco, Calif., 11–15 Dec.

Cardozo, N., Allmendinger, R.W., 2013. Spherical projections with OSXStereonet. Comput. Geosci. 51, 193–205. https://doi.org/10.1016/j.cageo.2012.07.021.

Chapman, T., Williams, G., 1984. Displacement–distance methods in the analysis of fold-thrust structures and linked-fault systems. J. Geol. Soc. Lond. 141, 121–128. https://doi.org/10.1144/gsjgs.141.1.0121.

Cowie, P.A., Scholz, C.H., 1992. Displacement–length scaling relationship for faults: data synthesis and discussion. J. Struct. Geol. 14 (10), 1149–1156. http://doi.org/10.1016/0191-8141(92)90066-6.

Davis, D., Suppe, J., Dahlen, F.A., 1983. Mechanics of fold-and-thrust belts and accretionary wedges. J. Geophys. Res., Solid Earth 88 (B2), 1153–1172.

DeCelles, P.G., DeCelles, P.C., 2001. Rates of shortening, propagation, underthrusting, and flexural wave migration in continental orogenic systems. Geology 29 (2), 135–138. http://doi.org/10.1130/0091-7613(2001)029<0135:ROSPUA>2.0.CO;2.

Gani, M.R., Alam, M.M., 1999. Trench-slope controlled deep-sea clastics in the exposed lower Surma group in the southeastern fold belt of the Bengal Basin, Bangladesh. Sediment. Geol. 127, 221–236.

Grall, C., Steckler, M.S., Pickering, J.L., Goodbred, S., Sincavage, R., Paola, C., Akhter, S.H., Spiess, V., 2018. Subsidence of the Ganges–Meghna–Brahmaputra delta plain during the Holocene. Earth Planet. Sci. Lett. 499, 23–36. https://doi.org/10.1016/j.epsl.2018.07.008.

Hardy, S., Ford, M., 1997. Numerical modelling of trishear fault-propagation folding and associated growth strata. Tectonics 16 (5), 841–854.

Hardy, S., Duncan, C., Masek, J., Brown, D., 1998. Minimum work, fault activity and the growth of critical wedges in fold and thrust belts. Basin Res. 10, 365–373. https://doi.org/10.1046/j.1365-2117.1998.00073.x.

Higgins, S., Clarke, B., Davies, R.J., Cartwright, J., 2009. Internal geometry and growth history of a thrust-related anticline in a deep water fold belt. J. Struct. Geol. 31, 1597–1611. http://doi.org/10.1016/j.jsg.2009.07.006.

Hubbard, J., Barbot, S., Hill, E.M., Tapponnier, P., 2015. Coseismic slip on shallow décollement megathrusts: implications for seismic and tsunami hazard. Earth-Sci. Rev. 141, 45–55. https://doi.org/10.1016/j.earscirev.2014.11.003.

Imam, M.B., Hussain, M., 2002. A review of hydrocarbon habitats in Bangladesh. J. Pet. Geol. 25 (1), 31–52. https://doi.org/10.1111/j.1747-5457.2002.tb00098.x.

Judge, P.A., Allmendinger, R.W., 2011. Assessing uncertainties in balanced cross sections. J. Struct. Geol. 33, 458–467. https://doi.org/10.1016/j.jsg.2011.01.006.

Kastens, K.A., 1991. Rate of outward growth of the Mediterranean accretionary complex. Tectonophysics 199, 25–50. https://doi.org/10.1016/0040-1951(91)90117-B.

Kimura, G., Hina, S., Hamada, Y., Kameda, J., Tsuji, T., Kinoshita, M., Yamaguchi, A., 2012. Runaway slip to the trench due to rupture of highly pressurized megathrust beneath the middle trench slope: the tsunamigenesis of the 2011 Tohoku earthquake off the east coast of northern Japan. Earth Planet. Sci. Lett. 339–340, 32–45. http://doi.org/10.1016/j.epsl.2012.04.002.

Kopp, C., Fruehn, J., Flueh, E.R., Reichert, C., Kukowski, N., Bialas, J., Klaeschen, D., 2000. Structure of the Makran subduction zone from wide-angle and reflection seismic data. Tectonophysics 329 (1–4), 171–191. https://doi.org/10.1016/S0040-1951(00)00195-5.

Lang, K.A., Huntington, K.W., Burmester, R., Housen, B., 2016. Rapid exhumation of the eastern Himalayan syntaxis since the late Miocene. Bull. Geol. Soc. Am. 128 (9/10), 1403–1422. http://doi.org/10.1130/B31419.1.

Lay, T., Kanamori, H., Ammon, C.J., Koper, K.D., Hutko, A.R., et al., 2012. Depth-varying rupture properties of subduction zone megathrust faults. J. Geophys. Res., Solid Earth 117, 1–21. https://doi.org/10.1029/2011JB009133.

Marrett, R., Allmendinger, R.W., 1990. Kinematic analysis of fault-slip data. J. Struct. Geol. 12 (8), 973–986. https://doi.org/10.1016/0191-8141(90)90093-E.

Maurin, T., Rangin, C., 2009. Structure and kinematics of the Indo-Burmese Wedge: recent and fast growth of the outer wedge. Tectonics 28 (2), 1–21. https://doi.org/10.1029/2008TC002276.

McCaffrey, R., Zwick, P.C., Bock, Y., Prawirodirdjo, L., Genrich, J.F., Stevens, C.W., Puntodewo, S.S.O., Subarya, C., 2000. Strain partitioning during oblique plate convergence in northern Sumatra: geodetic and seismologic constraints and numerical modelling. J. Geophys. Res. 105, 28,363–28,376. https://doi.org/10.1029/1999JB900362.

Mitra, S., Bhattacharya, S.N., Nath, S.K., 2008. Crustal structure of the Western Bengal basin from joint analysis of teleseismic receiver functions and Rayleigh-wave dispersion. Bull. Seismol. Soc. Am. 98 (6), 2715–2723. https://doi.org/10.1785/0120080141.

Mitra, S., Priestley, K.F., Borah, K., Gaur, V.K., 2018. Crustal structure and evolution of the Eastern Himalayan Plate Boundary System, Northeast India. J. Geophys. Res., Solid Earth 123 (1), 621–640. http://doi.org/10.1002/2017JB014714.

Mondal, D.R., McHugh, C.M., Mortlock, R.A., Steckler, M.S., Mustaque, S., Akhtere, S.H., 2018. Microatolls document the 1762 and prior earthquakes along the southeast coast of Bangladesh. Tectonophysics. https://doi.org/10.1016/j.tecto.2018.07.020.

Mueller, K., Suppe, J., 1997. Growth of Wheeler Ridge anticline, California: geomorphic evidence for fault-bend folding behaviour during earthquakes. J. Struct. Geol. 19 (3–4), 383–396. http://doi.org/10.1016/S0191-8141(96)00112-5.

Najman, Y., Allen, R., Willett, E.A.F., Carter, A., Barfod, D., Garzanti, E., Wijbrans, J., Bickle, M.J., Vezzoli, G., Ando, S., Oliver, O., Uddin, M.J., 2012. The record of Himalayan erosion preserved in the sedimentary rocks of the Hatia Trough of the Bengal Basin and the Chittagong Hill Tracts, Bangladesh. Basin Res. 24 (5), 499–519. http://doi.org/10.1111/j.1365-2117.2011.00540.x.

Najman, Y., Bracciali, L., Parrish, R.R., Chisty, E., Copley, A., 2016. Evolving strain partitioning in the Eastern Himalaya: the growth of the Shillong Plateau. Earth Planet. Sci. Lett. 433, 1–9.

Nielsen, C., Chamot-Rooke, N., Rangin, C., 2004. From partial to full strain partitioning along the Indo-Burmese hyper-oblique subduction. Mar. Geol. http://doi.org/10.1016/j.margeo.2004.05.001.

Park, J.-O., Tsuru, T., Takahashi, N., Hori, T., Kodaira, S., Nakanishi, A., Miura, S., Kaneda, Y., 2002. A deep strong reflector in the Nankai accretionary wedge from multichannel seismic data: implications for underplating and interseismic shear stress release. J. Geophys. Res., Solid Earth 107 (B4). https://doi.org/10.1029/2001JB000262. ESE 3-1–ESE 3-16.

Poblet, J., McClay, K., 1996. Geometry and kinematics of single-layer detachment folds. Am. Assoc. Pet. Geol. Bull. 80 (7), 1085–1109.

Rangin, C., Maurin, T., Masson, F., 2013. Combined effects of Eurasia/Sunda oblique convergence and East-Tibetan crustal flow on the active tectonics of Burma. J. Asian Earth Sci. 76, 185–194. https://doi.org/10.1016/j.jseaes.2013.05.018.

Rangin, C., 2017. Active and recent tectonics of the Burma Platelet in Myanmar. Geol. Soc. Mem. 48, 53–64. http://doi.org/10.1144/M48.3.

Rao, N.P., Kumar, M.R., 1999. Evidences for cessation of Indian plate subduction in the Burmese arc region. Geophys. Res. Lett. 26, 3149–3152.

Saito, S., Goldberg, D., 2001. Compaction and dewatering processes of the oceanic sediments in the Costa Rica and Barbados subduction zones: estimates from in situ physical property measurements. Earth Planet. Sci. Lett. 191 (3–4), 283–293. https://doi.org/10.1016/S0012-821X(01)00403-4.

Satyabala, S.P., 1998. Subduction in the Indo-Burma region: is it still active? Geophys. Res. Lett. 25 (16), 3189–3192.

Scholl, D.W., Kirby, S.H., Huene, R. Von, Ryan, H., Wells, R.E., Geist, E.L., 2015. Great (≥Mw 8.0) megathrust earthquakes and the subduction of excess sediment and bathymetrically smooth seafloor. Geosphere 11 (2), 236–265. https://doi.org/10.1130/GES01079.1.

Scholz, C.H., 1998. Earthquakes and friction laws. Nature 391 (6662), 37–42. http://doi.org/10.1038/34097.

Sibuet, J.C., Klingelhoefer, F., Huang, Y.P., Yeh, Y.C., Rangin, C., Lee, C.S., Hsu, S.K., 2016. Thinned continental crust intruded by volcanics beneath the northern Bay of Bengal. Mar. Pet. Geol. 77, 471–486. http://doi.org/10.1016/j.marpetgeo.2016.07.006.

Sikder, A., Alam, M., 2003. 2-D modelling of the anticlinal structures and structural development of the eastern fold belt of the Bengal basin, Bangladesh. Sediment. Geol. 155, 179–208.

Singh, A., Bhushan, K., Singh, C., Steckler, M.S., Akhter, S.H., Seeber, L., Kim, W-Y., Tiwari, A., Biswas, R., 2016. Crustal structure and tectonics of Bangladesh: new constraints from inversion of receiver functions. Tectonophysics 680, 99–112. http://doi.org/10.1016/j.tecto.2016.04.046.

Sloan, R.A., Elliott, J.R., Searle, M.P., Morley, C.K., 2017. Active tectonics of Myanmar and the Andaman Sea. Mem. Geol. Soc. Lond. 48 (1), 19–52. https://doi.org/10.1144/M48.2.

Steckler, M.S., Akhter, S.H., Seeber, L., 2008. Collision of the Ganges–Brahmaputra Delta with the Burma Arc: implications for earthquake hazard. Earth Planet. Sci. Lett. 273, 367–378. https://doi.org/10.1016/j.epsl.2008.07.009.

Steckler, M.S., Mondal, D.R., Akhter, S.H., Seeber, L., Feng, L., Gale, J., Hill, E.M., Howe, M., 2016. Deformation and seismic hazard associated with the Indo-Burman foldbelt from new GPS measurements in Bangladesh. Nat. Geosci. https://doi.org/10.1038/ngeo2760.

Suppe, J., Medwedeff, D.A., 1990. Geometry and kinematics of fault-propagation folding. Eclogae Geol. Helv. 83, 409–454.

Suppe, J., Connors, C.D., Zhang, Y., 2004. Shear fault-bend folding. In: McClay, K.R. (Ed.), Thrust Tectonics and Hydrocarbon Systems. In: AAPG Memoir, vol. 82, pp. 303–323.

Sun, T., Wang, K., Fujiwara, T., Kodaira, S., He, J., 2017. Large fault slip peaking at trench in the 2011 Tohoku-oki eartquake. Nat. Commun. 8, 1–8. https://doi.org/10.1038/ncomms14044.

Wang, Y., Shyu, J.B.H., Sieh, K., Chiang, H., Wang, C., et al., 2013. Permanent upper plate deformation in western Myanmar during the great 1762 earthquake: implications for neotectonic behavior of the northern Sunda megathrust. J. Geophys. Res., Solid Earth 118, 1277–1303. https://doi.org/10.1002/jgrb.50121.

Wang, Y., Sieh, K., Tun, S.T., Lai, K.-Y., Myint, T., 2014. Active tectonics and earthquake potential of the Myanmar region. J. Geophys. Res., Solid Earth 119, 3767–3822. https://doi.org/10.1002/2013JB010762.

Zahid, K.M., Uddin, A., 2005. Influence of overpressure on formation velocity evaluation of Neogene strata from the eastern Bengal Basin, Bangladesh. J. Asian Earth Sci. 25 (3), 419–429. https://doi.org/10.1016/j.jseaes.2004.04.003.